ELSEVIER

Nuclear Instruments and Methods in Physics Research A 487 (2002) 113–122

NUCLEAR INSTRUMENTS & METHODS IN PHYSICS RESEARCH Section A

www.elsevier.com/locate/nima

Charge sharing in silicon pixel detectors

K. Mathieson[a,*], M.S. Passmore[b], P. Seller[c], M.L. Prydderch[c], V. O'Shea[a], R.L. Bates[a], K.M. Smith[a], M. Rahman[a]

[a] *Department of Physics and Astronomy, University of Glasgow, Glasgow G12 8QQ, UK*
[b] *EP Division, CERN, Geneva, Switzerland*
[c] *Rutherford Appleton Laboratory, Chilton, Oxon OX11 0QX, UK*

Abstract

We used a pixellated hybrid silicon X-ray detector to study the effect of the sharing of generated charge between neighbouring pixels over a range of incident X-ray energies, 13–36 keV. The system is a room temperature, energy resolving detector with a Gaussian FWHM of 265 eV at 5.9 keV. Each pixel is 300 μm square, 300 μm deep and is bump bonded to matching read out electronics. The modelling packages MEDICI and MCNP were used to model the complete X-ray interaction and the subsequent charge transport. Using this software a model is developed which reproduces well the experimental results. The simulations are then altered to explore smaller pixel sizes and different X-ray energies. Charge sharing was observed experimentally to be 2% at 13 keV rising to 4.5% at 36 keV, for an energy threshold of 4 keV. The models predict that up to 50% of charge may be lost to the neighbouring pixels, for an X-ray energy of 36 keV, when the pixel size is reduced to 55 μm. © 2002 Published by Elsevier Science B.V.

Keywords: Charge sharing; Pixel detectors; Silicon; Simulation

1. Introduction

Semiconductor pixel detectors are used in many areas of science and research due to their low noise, high spatial resolution and 2-D position information. These properties have led to application in diverse fields including pixel detectors for medical imaging [1], X/γ-ray spectroscopy [2] and high energy particle detection [3].

Pixel detectors consist of an array of detection elements, and in the case of semiconductors the elements usually comprise diode structures. This array of diodes is either individually or globally coupled to readout electronics and can operate in a variety of modes, e.g. charge integrating or photon counting [4]. Such detectors fall into two broad categories: charge coupled devices (CCDs) and active pixel sensors (APS). CCDs are a matrix of diodes sequentially clocked out, by varying the potential applied to each element of the array, to a single pre-amplifier. They are commercially available, well understood and in common use. For a review of these devices see Damerell [5]. In APS each detection element has a dedicated electronic readout channel. This gives these devices many advantages over CCDs, principally high readout rate, the possibility of on-pixel processing and an increased dynamic range. Until recently the main drawback of the APS was the size of the pixel.

*Corresponding author. Tel.: +44-141-330-5894; fax: +44-141-330-5881.
E-mail address: k.mathieson@physics.gla.ac.uk (K. Mathieson).

0168-9002/02/$ - see front matter © 2002 Published by Elsevier Science B.V.
PII: S0168-9002(02)00954-3

However, recent advances in CMOS technology have led to APSs with pixel dimensions close to that obtained by CCDs. This paper will concentrate on charge sharing in active pixel sensors.

The need to reduce pixel size is driven primarily by the requirements for increased spatial resolution. In many areas of imaging, photographic film is still the standard due to the excellent spatial resolution achievable. Here the sub-micron sized silver halide crystals act as the photon detectors. The increased detection efficiency, instant picture, improved contrast and image processing offered by semiconductor pixel detectors gives reason for the change to this technology. However, electronic devices must offer pixel dimensions down to 50 μm to become an alternative. Spectroscopic detectors also benefit from the increased segmentation that pixel detectors offer, by reducing the capacitive noise of the detection elements and increasing the achievable readout rate.

At these dimensions it is possible that the fundamental physical interactions could cause an effect to detector performance. Interacting X-rays give rise to photoelectrons. These lose energy by scattering processes giving the resulting charge cloud a lateral dimension of a few microns which increases during charge transport due to diffusion. If the lateral broadening of the charge is significant in comparison with the pixel pitch, it could mean that a substantial amount of charge might be collected at a neighbouring pixel. For particle physics applications this is sometimes desired, since fitting to a cluster of "hit" pixels can improve the accuracy of the position resolution. However, in spectroscopy this sharing of charge degrades the quality of the obtainable spectra. Medical imaging devices also suffer since more incident particles must be rejected (to maintain the spatial resolution) if too much charge is shared. This could lead to an increase in the radiation dose to a patient.

The first step in understanding these problems is often through computer modelling, where the electronics industry has developed advanced software packages to accurately model devices under development. These simulation packages are ideally suited to modelling semiconductor detectors, though much of the previous work in this field uses non-commercial software [6–8]. One of the current limitations of detector modelling is in forming a complete picture of the particle interaction and the subsequent transport of charge. Often, only one of these physical processes can be simulated at a time. The fact that particle interactions are a statistical process means that many particles should be simulated and for each of the interactions a device simulation should be carried out. This leads to a prohibitive amount of computing time and so other approaches have to be considered. Here an attempt has been made to solve this problem by partially combining a Monte-Carlo particle transport code (MCNP 4C [9]) with a finite element electrical device simulator (MEDICI [10]).

The charge sharing effect has been analysed experimentally with a silicon active pixel sensor which has a pixel pitch of 300 μm. The amount of charge sharing was analysed using this detector over the energy range 13–36 keV and is shown to be in agreement with that expected from the models. The models have been extended to examine what effect charge sharing has on pixels of smaller dimensions and it is shown that as pixel dimensions approach 50 μm, the amount of charge sharing will significantly affect the properties of the pixel detector.

The experimental results were achieved using a spectroscopic pixel detector developed at the Rutherford Appleton Laboratories. The detector characteristics are reported here since the details have not yet been published elsewhere.

2. Experimental

2.1. The Dash-E detector

The Dash-E detector is the successor to the ERD1 detector system, technical details of which can be found in Ref. [11]. It is a charge-integrating detector that is intended for room temperature X-ray spectroscopy over the energy range 4–25 keV. The changes made to the ERD1 chip are an increased shaping time to 4 μs, a bipolar switch to allow electrons or holes to be collected at the readout electronics and a common mode which allows the whole detector to read out if one pixel records a hit. The other main change comes on the

front-end chip with the incorporation of an additional feedback capacitor in series allowing the capacitance of the front-end electronics to be switched to either 25 fF or 250 fF. This capability allows greater flexibility, as to the choice of detector medium and incident X-ray energy.

The detector is a 16×16 matrix of square pixel elements of pitch 300 μm. The pixels were fabricated on 3–10 kΩ cm, n-type, 4 in. silicon wafers, with the silicon crystal lattice orientated in the $\langle 1\,0\,0 \rangle$ plane (the wafer plane is perpendicular to this axis). The detector was designed to be illuminated through the n^+ ($n^+ = 10^{18}\,cm^{-3}$) ohmic contact. The p^+ ($p^+ = 10^{19}\,cm^{-3}$) boron implant on the pixellated side is connected to readout electronics via a gold stud bump bond.

2.1.1. Detector characteristics

Fig. 1 illustrates the spectral performance of the Dash-E detector. The pulse height spectra of fluorescent X-rays from Mn, Cu, Rb, Mo, Ag and Ba are shown on the same graph with the maximum counts normalised to one. The K_α and K_β lines from each element are clearly visible, and for the case of the Ba lines the $K_{\beta 1}$ and $K_{\beta 2}$ lines are separated. These measurements were taken at room temperature with no on-chip cooling. This is a single pixel response, but the whole matrix exhibits similar noise properties with the small variations in pixel to pixel gain being corrected by a software adjust as in the previous chip, which is detailed in Ref. [12].

Fig. 2 shows how the FWHM of the peaks in Fig. 1 change as a function of the incident X-ray energy. The total noise is shown alongside the contributions from the statistical variation in charge generation (the Fano factor contribution) and the electronic noise. The electronic noise was derived by operation of the detector in the "all" mode, where if a single pixel is hit all of the detection elements are read out. This means that the resultant spectrum contains not only the photopeaks of the incident spectrum but also a noise peak from the pixels that did not have an X-ray incident upon them. This Gaussian shaped noise peak was examined for the case of Mo X-rays and a value of 229.7 ± 6.6 eV was obtained for the FWHM. If the Fano and electronic contributions are added together in quadrature then the resultant line should fit the experimental data, provided there are no other sources of noise. It can be seen in Fig. 2 that this line is not a good fit to the noise and that there is another noise component which is sometimes contributed to charge collection problems [13], though full charge collection is expected in detectors of this type. The additional noise component follows closely the curve of the Fano factor component.

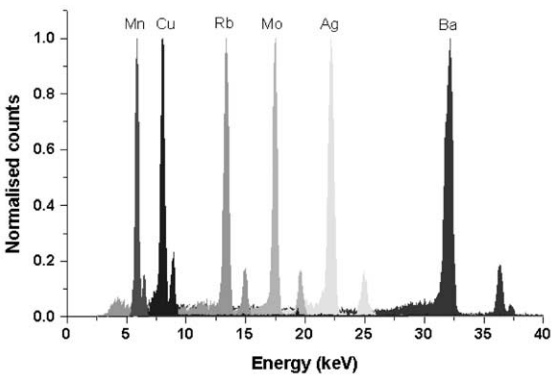

Fig. 1. Spectral response of the Dash-E silicon pixel detector.

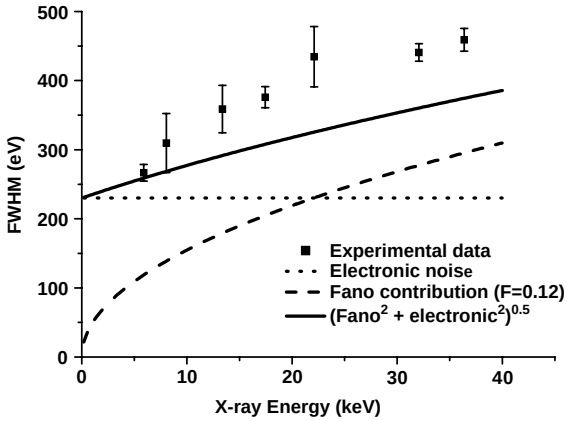

Fig. 2. The variation of FWHM with incident X-ray energy. The electronic noise and the Fano factor contributions are shown.

2.1.2. Charge sharing—experimental

The Dash-E detector is well suited to studying the phenomenon of charge sharing, since it has the ability to read out the output voltage in every pixel cell when one pixel registers an incident photon. This allows the analysis of not only the hit pixel but also of the surrounding pixels. Data of this format were taken for the X-ray lines of Rb, Mo, Ag and Ba. Since a low energy threshold of 4 keV has to be set in order to exclude electronic noise injection, charge sharing studies of Mn and Cu are not possible with this detector. During the experimental recordings care was taken to make sure that the detector to source separation was sufficient that the X-ray rate at the detector was low. The detector output was then monitored to ensure that only one X-ray photon was incident upon any one pixel during that readout cycle. The steps that follow describe the analysis that each data set undergoes.

- The data set is read into a C-program where all of the pixel offsets are subtracted by the use of a calibration file. This corrects for an offset in the output voltage on a pixel to pixel basis.
- The maximum value of each readout cycle is selected as the hit pixel.
- The eight surrounding pixels and the hit pixel are then selected from each readout cycle.
- An upper energy threshold value is then set to a value of 1 keV above the K_β peak of the chosen spectrum. All hits above this value are discarded since here we only want to consider hits from the selected spectrum. Discarded hits will arise from the 60 keV ^{241}Am γ-rays.
- The charge shared to the surrounding pixels is expressed as a percentage of the total charge.
- A threshold is set at low energy since every pixel will have an associated noise.
- The data are output to file for a scan of this lower threshold—from zero to the photopeak. The data comprises the fraction of charge shared events as a function of cut-off threshold. A graph of this data can be seen in Fig. 9.

As a check to ensure that charge shared events are being considered and not spurious or coincident hits, the information selected from the Mo dataset is shown in Fig. 3. This shows the events that have been selected by the C-program alongside the resultant spectrum, where the signal from the neighbouring pixel with which charge is shared is added to that from the hit pixel. Here the spectrum has effectively been corrected for charge sharing.

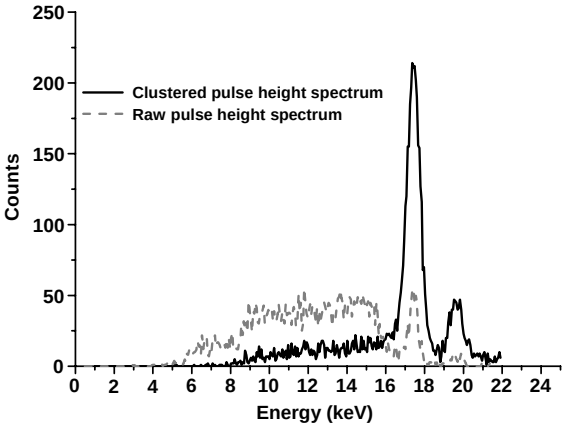

Fig. 3. The charge shared data from the Mo dataset, showing the raw data and the spectrum adjusted for charge sharing (clustered). The raw data corresponds to data in which a charge-shared event has occurred but no correction has been performed. The clustered data is the same data but this time the charge sharing correction has been included.

This illustrates firstly that charge sharing takes place and that it results in a reduction of the photopeak intensity and an increase in the background level. It can also be seen in the selected data that some counts have escaped the cuts since a K_α peak is visible in the unadjusted data. This accounts for about 10% of the total counts.

3. Modelling

3.1. Photon transport

A detailed 3-D model of the Dash-E detector was created within the modelling package MCNP. It included the silicon detection element, the silicon readout electronics and the bump bond complete with the metallisation layers. This pixel was arrayed in a 16×16 matrix to form a complete model of the detector. MCNP requires the atomic number and the ratios of the constituent elements in addition to the geometry and source definitions.

The source–detector set-up was described as a point source emitting photons directed down a line through the centre of one of the pixels. The energy deposited in the whole detection volume (a cube with 300 μm sides) is then "tallied". The source data contains all of the known spectral lines for each of the sources used in the experimental work and are taken from the tables in Ref. [14].

Fig. 4 shows the comparison of a barium spectrum taken with the Dash-E detector and the output from the MCNP model. A feature of MCNP is the incorporation of a Gaussian energy broadening term that accounts for spectral broadening due to the noise of the system. Fig. 2 shows how the noise of the Dash-E varied with incident X-ray energy. It is a fit to these data points that act as an input to the model.

The two most prominent differences between the model and experiment are the differences in the photopeak height and the background counts. The model and experiment have had the height of the $K_{\beta 2}$ peaks fixed to equal values. This peak was chosen since the effect of the background on this peak will be small in comparison to the K_{α} peaks. The expected K_{α} photopeak has 13% more counts than the experimental equivalent. Part of this discrepancy will be due to charge sharing between pixel elements, since the model at this stage does not take this into account—later it will be shown that charge sharing alone cannot account for the loss of counts in the photopeak.

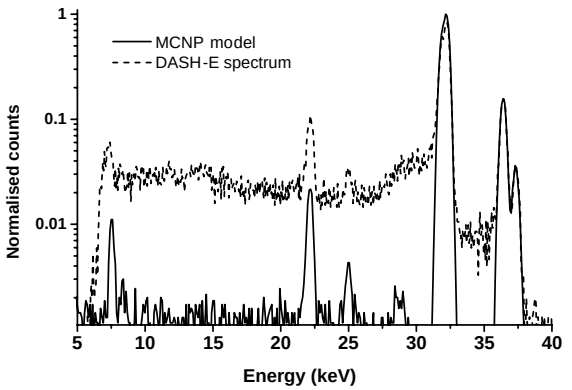

Fig. 4. A comparison of a barium spectrum from a modelled Dash-E detector and the experimental output.

Fig. 4 emphasises the differences between the two spectra because of the logarithmic y-axis. However, many of the aspects of the dash-E detector system have been reproduced by the model, such as the silver fluorescent lines at 22 and 25 keV which result from the silver epoxy layer needed during the assembly stage. The increased background level is expected to be a contribution from the readout electronics and so would naturally not be seen in the model. Nevertheless, Fig. 4 shows that the model is a good representation of the Dash-E detector and lends credence to the simulated data that is extracted from the model and used to model charge sharing.

The ideal method of studying charge sharing through modelling would be to transport one photon, calculate the generated charge distribution in the device and then apply the electrical simulation which transports the charge cloud through the detector. This would have to be repeated many times to ensure good statistics, just as a large number of counts are needed to ensure a good experimental pulse height spectrum. The computational time for this type of modelling is at present prohibitive and so alternative approaches have to be developed.

The approach adopted here separates the photon transport and energy loss, from the electron–hole transport. The MCNP model described above yields the averaged energy deposition of many particles. So a map of the most likely position for photons, from a particular source, to deposit their energy is created. This data was extracted for the Rb, Mo, Ag and Ba spectra and can be incorporated into MEDICI for the charge transport.

3.2. Charge transport

Up to now no drift or diffusion effects have been considered in the models. To do this the finite element device simulator MEDICI was used. MEDICI self-consistently solves both Poisson's equation and the continuity equations for electrons and holes. The models included in the simulations are impact ionisation, the incomplete ionisation of donors and acceptors, Shockley Read Hall statistics and Auger recombination. The

output from MCNP is used to give the charge generation points in MEDICI; these data describe the energy deposition for an average of many photons emitted from a point source. So their incorporation into MEDICI means that many photo-generated charge clouds will be drifted through the detection medium in a single device simulation. For this to be valid the charge density of the generated carriers must be below that at which carrier–carrier interactions become important. Experimentally this density has been observed to be far above that of the charge carrier density here [15]. Since MCNP is a 3-D code and MEDICI is 2-D, we use a projection to approximate the 3-D distribution. The energy deposition from MCNP is extracted in a 1 μm slice through the detection material giving the energy density distribution in 2 dimensions. This profile is then created within MEDICI where the model has the same doping densities, implants and operating voltages as the experimental case (the Dash-E detector operating at 80 V reverse bias). A key aspect of the charge transport is ensuring that the width of the modelled semiconductor is such that no charge is reflected at the Neumann boundaries (where the E-field perpendicular to the surface goes to zero). This is the unalterable default setting for all surfaces not in contact with an electrode in MEDICI, and will change the charge distribution at the contact if not accounted for.

The charge distribution that is the result of the MEDICI simulation takes into account the following effects :

- The source characteristics—spectral lines and relative intensities
- The multiple scattering of the photoelectron and fluorescent contributions in 300 μm silicon (MCNP data).
- The drift and diffusion of the carriers in the detector geometry (MEDICI data).
- The operating conditions of the Dash-E detector (80 V reverse bias at room temperature).

The profiles for the four sources tested are shown in Fig. 5 where the maximum of each curve is normalised to unity for comparison. Fig. 5 illustrates that as the energy of the interacting energy increases so does the width of the charge distribution, which in turn implies increased charge sharing.

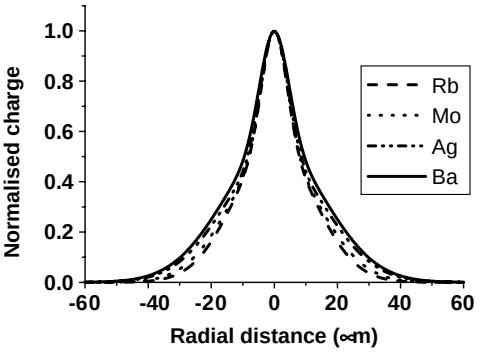

Fig. 5. The normalised charge distributions for each source after transport through modelled Dash-E detector.

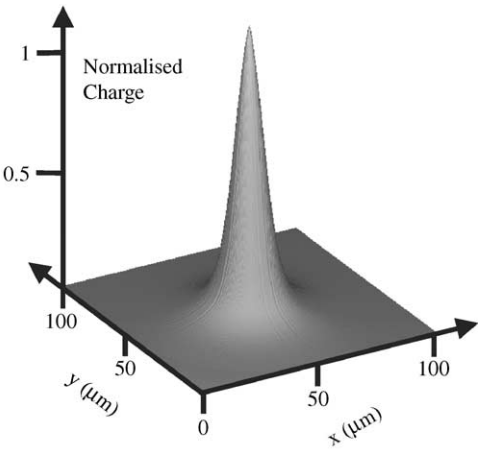

Fig. 6. The radial distribution, after charge transport, rotated around the charge generation point.

If the Gaussian profiles shown in Fig. 5 are rotated around 180°, a cone will be formed which represents the charge profile of an X-ray interaction in 3 dimensions (see Fig. 6). This 3-D profile is the averaged response to a point source of X-rays illuminating a pixel detector of the Dash-E type.

To analyse charge sharing this new profile has to be integrated over the width and length of the pixel. Therefore, the contribution from point sources integrated over the pixel dimensions gives the response of a uniformly illuminated pixel.

Since the pixel boundaries are known, any charge that is outside these boundaries is lost to the neighbouring pixels. A plot of this integration over pixel width and length, of the distribution of Fig. 6, for a square pixel of pitch 300 μm is shown in Fig. 7. Here the dotted line indicates the boundary of the pixel and the charge lying outside this boundary is lost to the surrounding pixels.

4. Results

4.1. Comparing experiment with simulation

Fig. 9 shows experimentally how the amount of charge shared varies with the position of the minimum energy threshold. The amount of charge shared, calculated by the modelling analysis just described, gives one value for charge shared corresponding to a threshold of zero. So it is the maximum amount of charge that can be shared for that X-ray energy and at these pixel dimensions. However, experimental detector systems always have a low energy threshold that eliminates the noise of the system. Since this threshold ignores any amount of charge that is below it in value, it has an impact on how much charge sharing is seen by the detector system. To compare the modelled results with the experimental data requires a threshold dependence to be introduced. Three-pixel events were studied by the authors and were observed to occur $<1\%$ of the time and so are ignored in this analysis. This means that when a hit pixel is selected it always has at least 50% of the charge deposited by the interacting particle. So no charge sharing will be observed when the threshold is set to half that of the incident X-ray energy. Low energy photons will appear in the hit pixel, but the threshold in the neighbouring pixels will be too high to observe the shared charge. Fig. 8 illustrates more clearly the method used to achieve the threshold variation in the simulated case. This is a 2-D cut through the charge distribution under a pixel (i.e. a 2-D slice through the middle of Fig. 7) with the y-axis corresponding to the amount of charge generated normalised to unity. For uniform illumination the maximum amount of charge (Q_{max}) that can be collected below that pixel is that contained in the volume of the cuboid

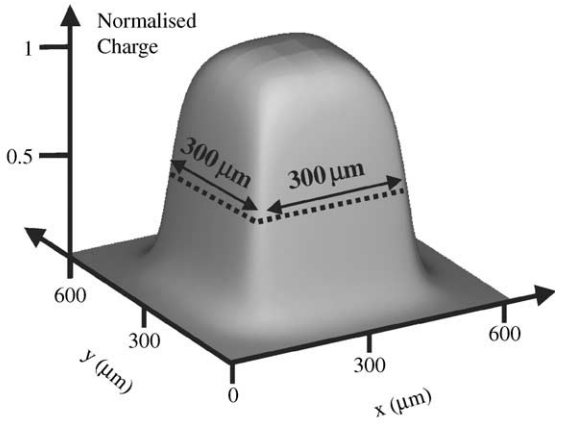

Fig. 7. Integration of charge response over pixel width and length for a square pixel of 300 μm side.

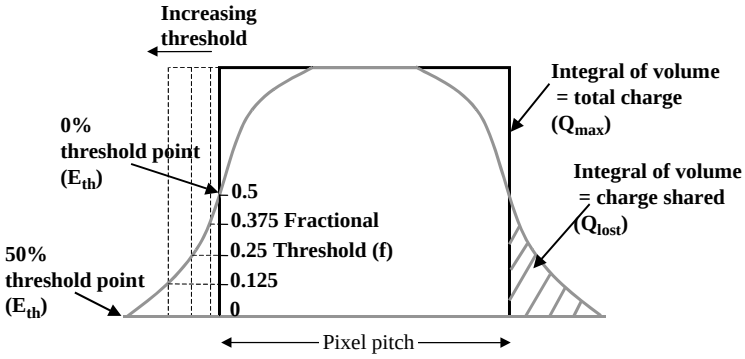

Fig. 8. Illustration of method for the calculation of how the modelled charge sharing depends upon the low energy cut-off threshold.

indicated by the solid thick line (height equal to unity, other sides equal to pixel pitch). This would be the distribution if there were no scattering or diffusion effects. The solid line indicates the distribution that has been spread out due to the scattering and diffusion processes inherent in solid state X-ray detection. The area of the charge outside the pixel boundaries is the amount of charge lost (Q_{lost}) but is converted to a volume when considering the distributions of Fig. 7—as was done here. The fraction of charge sharing is then the ratio $Q_{\text{lost}}/Q_{\text{max}}$, for a threshold of zero. The integration over the charge shared volume (indicated in Fig. 8) from the pixel boundary outwards corresponds to the zero threshold level and what is denoted as a fractional threshold value of 0.5. If the integration starts at a further out point along the curve of lost charge, the corresponding fractional threshold, denoted f, is linked to the threshold energy, $E_{\text{threshold}}$, by the equation $E_{\text{threshold}} = (1/2 - f)E_{\text{photon}}$. When the fractional threshold reaches zero the threshold energy is equal to half the incident photon energy, since the maximum charge shared corresponds to a 50–50 split. The results are the lines shown in Fig. 9 where they are compared with the experimental data from the Dash-E detector.

4.2. Discussion

Fig. 9 shows the output of the data analysis—the percentage of charge shared, detected at the neighbouring pixel, as a function of threshold energy. As expected the charge shared goes to zero at half the energy of the principle photopeak, since a 50% split is the maximum amount of charge that can be shared. At a threshold below 4 keV the noise from the system begins to enter into the charge shared events, so the experimental data below this point hold no real information. The experimental data points extend back to 2 keV to illustrate the effect the noise has on deviating the data from the simulated case. It can be seen that the amount of charge shared increases with energy over the range tested. For example if we consider an energy threshold of 4 keV we have 2.0% charge loss for Rb, rising to 3.4% at Mo, 4.0% for Ag and 4.5% at Ba. This increase is to be expected,

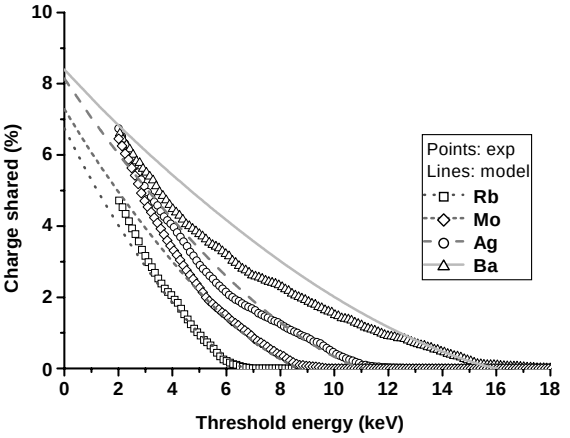

Fig. 9. Comparison of simulated and experimental results of charge sharing, as a function of energy threshold, for the Dash-E detector.

since the energy of the photoelectron increases with incident X-ray energy.

Since the two principle physical processes are handled by separate modelling codes we can isolate the effects of the scattering of the photoelectron and the fluorescent photons contribution (MCNP code) from the diffusion of the charge carriers in the semiconductor (MEDICI code). This allows the charge sharing process to be attributed to a particular effect. Repeating the analysis above but excluding the charge transport section allowed only the physics included in the MCNP code to be analysed. This was performed for the X-ray energies of Rb, Mo, Ag and Ba and a threshold of zero. A breakdown of the effects can be seen in Table 1.

5. Conclusions

As can be seen the simulations and the experimental data agree reasonably. Barium is the only set of X-ray lines that show a slight disagreement over the mid-range of threshold values. The deviation at low threshold values in all of the X-rays examined is due to the noise of the Dash-E system. This leads to spurious charge shared events when the threshold (observed here to be below 4 keV) is too low. Table 1 shows that the

Table 1
A breakdown of charge sharing effects for the modelled Dash-E detector, for the case of no low energy threshold

Energy of K_α (keV)	Charge sharing—no diffusion (%)	Charge sharing—diffusion included (%)	Difference (%)
13.34	0.72	6.7	5.98
17.44	0.9	7.3	6.35
22.1	1.2	8.1	6.9
32.06	2.1	8.4	6.3

dominant physical effect in charge sharing is the diffusion of the charge carriers and not the interaction of the photoelectron. This means that charge sharing could be reduced by increasing the operating voltage of the device and so the internal electric field. This gives the charge less time to diffuse. Materials with higher drift velocities such as GaAs should suffer less from charge sharing effects.

The models can also be extended to examine other detectors and used as a design tool to predict charge sharing effects in detectors not yet built. For example new highly pixellated silicon detectors are under design with a pixel pitch of 55 μm [16]. This detector will be a photon counting detector intended for imaging. When the models are applied to a detector of this type then a substantial amount of charge sharing is predicted, see Fig. 10. If these detectors were looking at monoenergetic X-rays then a threshold could be placed at 50% of the X-ray energy, and no charge shared events would be observed. The number of hits recorded would not be affected and there would be no blurring of the image. Unfortunately detectors such as these have potential medical imaging applications where commonly a Bremsstrahlung continuum is used as the source. This means that the higher energy X-rays will be present and threshold tuning will not eliminate the charge shared events from the high energy part of the Bremsstrahlung spectrum. In order to minimise charge sharing and maintain image quality a high electronic threshold would have to be set on the detector. This leads to information loss, which would require an increase in dose (detrimental to the patient) to compensate. Though the overall increase in interaction probability of X-rays in these detectors means they might still out-perform the existing technologies.

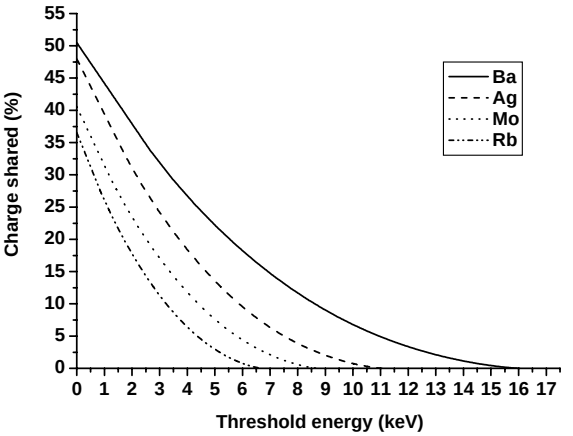

Fig. 10. New imaging detectors plan to use 55 μm square pixels on 300 μm thick silicon. The models indicate a substantial amount of charge will be shared with neighbouring pixels.

In the future it is anticipated that the models will be extended to include a 3-D modelling code that will handle the charge transport, to ensure that no 3-D effects are being ignored.

Acknowledgements

Thanks are due to Dr. Scott Roy and Professor Asen Asenov, of the device modelling group at the University of Glasgow, for allowing access to the MEDICI computing code and for helpful assistance.

References

[1] J.P. Moy, Nucl. Instr. and Meth. A 442 (2000) 26.

[2] P. Seller, et al., Silicon pixel detector for X-ray spectroscopy, SPIE 3445, EUV, X-ray and Gamma-ray Instrumentation for Astronomy IX, 1998, p. 584.
[3] C.J.S. Damerell, Vertex detectors: the state of the art and future prospects, Rutherford Lab preprint RAL-P-95-008, 1995.
[4] P. Seller, et al., Two approaches to hybrid X-ray pixel array readout, SPIE 3774, Detectors for Crystallography and Diffraction Studies at Synchrotron Sources, 1999.
[5] C.J.S. Damerell, Rev. Sci. Instrum. 69 (4) (1998) 1549.
[6] T.J. Brodbeck, A. Chilingarov, Nucl. Instr. and Meth. A 395 (1997) 29.
[7] A. Cola, et al., Appl. Phys. Lett. 73 (12) (1998) 1709.
[8] P. Sellin, Nucl. Instr. and Meth. A 434 (1) (1999) 75.
[9] J.F. Briesmeister (Ed.), MCNP—A General Monte Carlo N-Particle Transport Code, Los Alamos National Laboratory Report LA-13709-M, April, 2000.
[10] MEDICI, 4.1, AVANT! Corporation, 1998.
[11] P. Seller, et al., Nucl. Instr. and Meth. A 477 (2002) 161.
[12] S. Passmore, Pixel detectors, Ph. D. Thesis, University of Glasgow, G12 8QQ, Scotland, 2001.
[13] G.F. Knoll, Radiation Detection and Measurement, Wiley, New York, 1979.
[14] R.B. Firestone, Table of Isotopes, 8th Edition, Wiley, New York, 1999.
[15] F. Nava, et al., Nucl. Instr. and Meth A 426 (1999) 185–191.
[16] MEDIPIX Collaboration, Information available from http://medipix.web.cern.ch/MEDIPIX/.